ADVANCED MATERIALS INTERFACES
www.advmatinterfaces.de

Au(111) Surface Contamination in Ambient Conditions: Unravelling the Dynamics of the Work Function in Air

Nicholas Turetta, Francesco Sedona, Andrea Liscio, Mauro Sambi, and Paolo Samorì**

Gold is an inert noble metal displaying superior chemical stability that renders it a suitable component for the manufacturing of electrodes for various types of devices. Despite being widely employed, the variation of gold surface properties occurring upon the material's exposure to ambient conditions have been often disregarded. While it is well-known that the contamination of a metallic surface can have a dramatic impact on its properties, the process of contamination itself is poorly understood. Changes of the work function by fractions of an electron-volt are commonly observed in gold surfaces that are processed at ambient laboratory conditions, but an exhaustive comprehension and control of this phenomenon are still lacking. Here, a multiscale characterization of Au(111) surfaces aiming to unravel the surface dynamics underlying the air contamination is presented. The visualization of the adventitious carbon contamination on Au(111) surface by atomic force microscopy is key to rationalize the mechanisms of surface reorganization ruling the change of Au work function between 5.25 and 4.75 eV by solely changing the storage conditions. Such a huge variation must be taken into account when optimizing the Au surface for both controlling its fundamental surface and interfacial physical processes, as well as its functional applications.

1. Introduction

Gold is classified as a noble metal by virtue of its resistance to corrosion and oxidation. Clean gold is characterized by a hydrophilic and high-energy surface, but, despite its inertness, the clean surface gets contaminated with small organic molecules within a few minutes of exposure to ambient air.[1] In fact, the so-called adventitious carbon (AdC)[2] is ubiquitously present on the surface of inorganic materials, such as metals,[3] silicon dioxide,[4] or indium tin oxide (ITO).[5] This airborne contamination is known to form a layer that changes the wettability of these surfaces rendering them hydrophobic upon air exposure.[1,6] Gold is widely employed both in applied and fundamental research (e.g., optoelectronic device fabrication, adsorption studies, and electrochemical detection) and it is also a suitable material for gravitational waves detection (Gravity Probe B,[7] UV-LED,[8] and LISA Pathfinder[9]). The control of adventitious contamination is of critical importance for the above-cited applications, as surface cleanliness and uniformity are among the key requirements to obtain reliable and reproducible results.[10] For example, in ultrahigh vacuum (UHV) environments, sputter-cleaning via ion-gun bombardment followed by thermal annealing is used to remove organic contaminants to yield clean metallic surfaces.[11] Alternatively, thin films of pure gold can also be produced in situ via thermal evaporation,[6c,12] sputtering deposition[13] or e-beam evaporation,[13a] in high vacuum (HV). If gold surfaces are processed at ambient pressure (e.g., used as a substrate for the deposition of thin films or for the adsorption of biomolecules, monolayer films, or nanoparticles) cleaning and/or pretreatment protocols are often necessary, even for freshly evaporated metals.[12] Different combinations of dry treatments (e.g., flame annealing,[14] plasma cleaning,[15] ultraviolet/ozone (UV/O_3),[16] and mechanical polishing[17]) and wet treatments (e.g., rinsing and/or ultrasonication in a cleaning solvent and (electro) chemical treatments[17,18]) are commonly employed during the early stages of sample preparation prior to further processing. Residual contamination or structural changes induced by the treatment might influence, for instance, the electrochemical response of gold, still without completely preventing its functionality.[18b] In other cases, instead, as in surface force or molecular adsorption studies done via scanning probe microscopy (SPM),[10a] a very smooth and clean surface is required. The AdC contamination usually represents the uppermost layer and its presence heavily affects the measurement of surface-sensitive physical properties; for example, Gomez-Herrero and co-workers[19] showed via Kelvin probe force microscopy (KPFM) that carbon contamination can locally change the work function (WF) of a highly oriented pyrolytic graphite (HOPG) sample (freshly cleaved in ambient air and transferred inside a

N. Turetta, Prof. P. Samorì
Université de Strasbourg
CNRS
ISIS UMR 7006, 8 allée Gaspard Monge, Strasbourg F-67000, France
E-mail: samori@unistra.fr
N. Turetta, Prof. F. Sedona, Prof. M. Sambi
Dipartimento di Scienze Chimiche
Università degli Studi di Padova
Via Marzolo 1, Padova 35131, Italy
E-mail: mauro.sambi@unipd.it
Dr. A. Liscio
Istituto per la Microelettronica e Microsistemi (IMM)
Unità di Roma
Consiglio Nazionale delle Ricerche (CNR)
Via del Fosso del Cavaliere 100, Rome 00133, Italy

The ORCID identification number(s) for the author(s) of this article can be found under https://doi.org/10.1002/admi.202100068.

DOI: 10.1002/admi.202100068

vacuum chamber at the pressure of 1×10^{-5} mbar) by ≈0.2 eV. Ideally, the complete removal of AdC is required for the correct determination of the WF by means of ultraviolet photoelectron spectroscopy (UPS), especially when relatively small WF variations are expected (e.g., differences arising from crystallographic orientations of Au[20] and Ag[21] single crystals). However, the removal of the AdC layer often implies the transfer of the sample in a UHV environment and the invasive cleaning (e.g., via sputtering) can cause a major modification of the surface structure. Hence, with the aim to characterize the system in conditions as similar as possible to those of working devices, macroscopic Kelvin probe (KP) and photoelectron yield spectroscopy (PYS) are widely employed to estimate the WF or the ionization potential (IP) of materials in ambient atmosphere.[22] In addition, in order to preserve the integrity of the sample, surface analyses can be performed without removing the AdC layer and correction models are employed for data analysis, as in X-ray photoelectron spectroscopy (XPS)[4a,23] and X-ray reflectometry (XRR).[4d,24] While many efforts have been dedicated to the removal of the AdC layer, the process of contamination itself is still poorly understood. The evolution of the surface properties of a metallic sample during ambient exposure is overlooked as well, despite large changes being observed depending on the preparation conditions and the environmental history of the sample.[25] Each storage, processing, or cleaning step might also affect the surface properties such as work function,[16b,25b,26] wettability,[10a,15a] and surface composition.[11a,16b,27] During the experimental practice, the identification of the source(s) of contamination is highly sought after. Since the formation of the AdC layer is a direct consequence of the exposure of the sample to a complex medium, i.e., ambient air, a plethora of different volatile species are interacting with the surface. An analytical and rational approach studying the adsorption and desorption of specific compounds[28] fails to comprehensively describe the actual dynamics of surface contamination. Instead, a more accurate description of the system could be achieved if the structure and morphology of the contamination layer could be determined experimentally. SPM techniques, such as atomic force microscopy (AFM), scanning tunneling microscopy (STM), and KPFM, can provide direct insight into local changes of the surface properties. In principle, the presence of an AdC superficial layer could be detected with these techniques and its properties mapped as 2D grids of data points. However, many complications are associated with the characterization of contamination in general. For instance, if the contamination layer has a uniform thickness, chemical composition, and spatial distribution, only limited information can be extracted from surface imaging even at the best operating conditions of the instrument, thereby rendering the contamination undistinguishable from the substrate. In addition, the distinction between features arising from surface contamination and features peculiar to the clean surface is further hindered in samples characterized by a corrugated surface (e.g., polycrystalline Au with randomly oriented crystallites). Conversely, the surface of Au(111) on mica can exhibit atomically flat terraces, which can serve as ideal platforms to study the dynamics of AdC contamination.

In this work, we present the dynamics of surface contamination of Au(111) grown on mica substrates upon exposure to ambient air. The evolution with time of the experimental work function during the contamination process was compared with the trend of the other surface properties. Two separate regimes were identified and rationalized by means of surface characterization techniques. The growth of the AdC contamination layer, due to the continuous accumulation of airborne contaminant species, was monitored via AFM, revealing its tendency to form nanometric aggregates, which diffuse and merge, thereby affecting the properties of the Au surface at different length scales. In particular, we found that the AdC contamination determines large variabilities in the WF of the Au samples (e.g., for polycrystalline Au the WF is found to range between 4.4 and 5.4 eV depending on the preparation conditions).[25a,29] Toward this end, we finally unveil the mechanism governing the variation of the WF of Au(111), which occurs in a range of 0.5 eV and whose extent depends on the storage environment and time. The WF can also be reversibly changed within this range by storing the sample in an open air container or in a sealed container placed in the same room. The unprecedently reported phenomenon of contaminant aggregate dynamics elucidates the long unexplained question of the work function of gold, which troubled the surface science community for decades.

2. Results and Discussion

2.1. KP and PYS Measurements

The macroscopic WF and contact potential difference (CPD) changes occurring upon aging of Au(111) samples during exposure to ambient conditions were assessed via PYS[30] and KP,[31] respectively. We recorded the WF and CPD versus time curves of template-stripped (TS) Au(111) samples, shown in **Figure 1**a. Mica TS Au(111) thin films are often used as a clean hydrophilic surface,[1,10a] thus its characterization is interesting both from a fundamental and an applicative perspective. The measured WF and CPD show a similar trend: i) a fast decrease in the first 15 min reaching the minimum after about 60 min, and ii) a subsequent slow and partial recovery of the initial values due to an equilibration process, which involves the gold surface and its contamination layer. Remarkably, both the WF and the CPD of Au(111) were found to change in a range of 0.5 eV within the first 2 h of exposure to ambient conditions, in a range of values comparable to those detected by Kahn and co-workers via UPS analysis.[3b] The fast WF decrease started from values slightly below those of sputter-cleaned (SC) Au(111), determined to be 5.30 ± 0.05 eV in UHV.[20] A similar decrease in WF was also observed by Kinoshita et al.[32] as a function of the AdC coverage of Au samples in UHV. The CPD and WF were then monitored at longer timescales on the very same sample, as shown in Figure 1b. The slow overall increase of the CPD (i.e., few tens of mV per day) indicates that the equilibration process of the gold surface with the environment requires days or weeks to be completed. After one month of continuous exposure to the ambient atmosphere, the CPD was found not to increase further, thereby reaching a plateau. The reliability of such measurement, also in terms of long-term stability of the tip WF (WF_{tip}), was guaranteed by two reference samples: a freshly exfoliated HOPG sample and a Au(111) on mica sample that was stored inside the open air KP setup, in close proximity

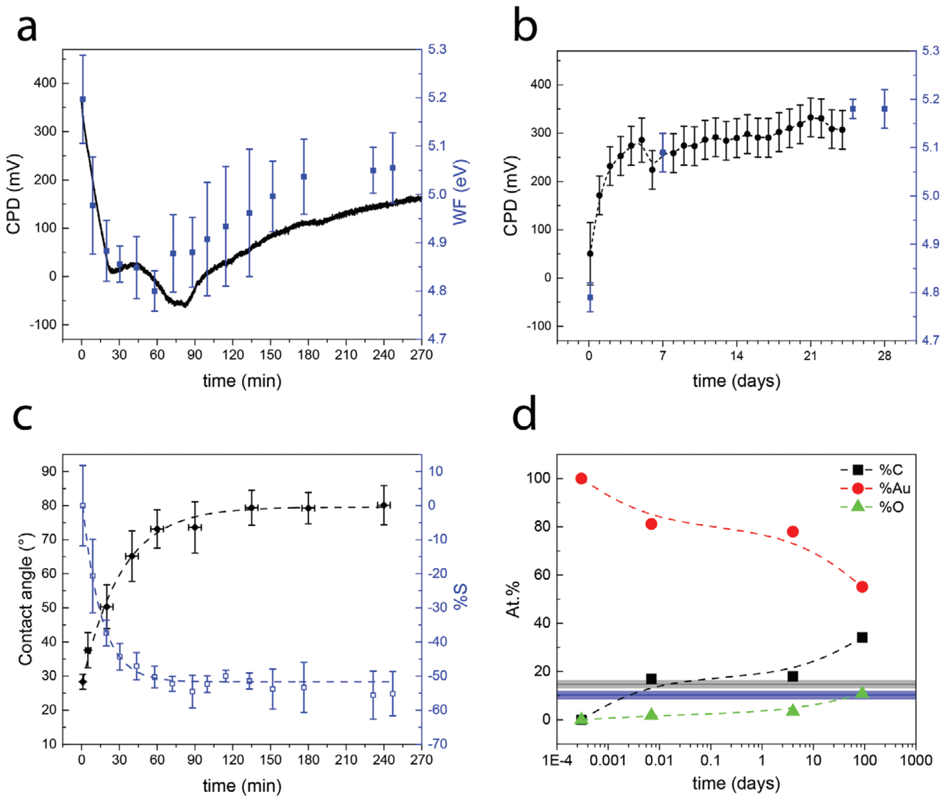

Figure 1. Surface properties (WF, CA, AdC layer, and atomic composition) of clean Au(111) as a result of the exposure to laboratory environment for different time periods. a) Short- and b) long-term WF and CPD measurements. a) Example of CPD (black solid) curve, determined by KP, versus average WF data (blue squares), determined by PYS, collected from TS Au(111) thin films at ambient conditions. The reported photoelectric WF values were estimated from the onset of photoelectron yield (PY) Fowler plots. The tip calibration for CPD measurements is $WF_{tip} = 4.83$ eV. b) Long-term acquisition of CPD data (black circles) versus PYS WF data (blue squares) from the same Au(111) on mica sample during exposure to ambient air. c) AdC layer formation: contact angle (black squares) versus relative decrease of PY slope (%*S*, blue empty squares). d) Au surface composition: atomic percentage of the most abundant elements on an air-contaminated gold surface extrapolated from XPS analysis of Au 4f, C 1s, and O 1s peaks as a function of time (semilogarithmic scale). The surface composition of the sample cleaned in UHV is assigned to a finite time value for convenience. Compositional data was then collected after 10 min, 4 days, and 3 months of aging at ambient conditions. The blue horizontal dashed line and the light blue area represent the average and standard deviation of the %C value of a 0.7 PPP monolayer (see text) on Au(111), 11 ± 2%, while the gray solid line and area represent the same value after correction for a complete PPP monolayer, 16 ± 2% (see Section S2 in the Supporting Information).

to the tip (calibration data are reported in Figure S1a in the Supporting Information).

To rationalize the physics underlying the observation of two distinct regimes of WF variation, a comprehensive understanding of the AdC layer formation and surface dynamics is required. A first evidence of the AdC layer formation is given by the time evolution of the slope of the photoelectron yield (PY) Fowler plots (examples reported in Figure S1b in the Supporting Information), which is known to be correlated to the thickness of the contamination layer.[33] By monitoring the relative decrease of the PY slope (%*S*), it is possible to obtain an indirect proof of the formation of the AdC layer, as shown in Figure 1c. A second evidence is provided by the change in the surface wettability, induced by the formation of the contaminant layer, as evidenced by the water contact angle (CA) increase over time. Noteworthily, a similar increase in the water CA versus time curve was previously reported by Chai and Klein.[10a] The CA and %*S* curves in Figure 1c, decaying at a similar rate, assume an almost constant value within 2 h, suggesting that the increased hydrophobicity of the gold surface is correlated to the adsorption of airborne contaminant species. These experimental observations indicate that the dominant mechanism governing the change of the WF during the first hour of aging is the formation of a contamination layer. This WF change can be described in terms of the "pillow effect:" the presence of adsorbates on the metal surface leads to a compression of the surface electronic dipole, thus lowering the WF.[25a] While the rapid initial decrease in CPD is limited to the first 15 min, the bump in the CPD curve (obtained between 15 and 45 min) might indicate the temporal boundary between the rapid formation of a kinetic monolayer of contamination and its subsequent structural rearrangement into a more stable layer.

In general, the precise molecular composition of AdC strongly depends on the storage environment and on chemical nature of the contaminated sample.[2d,34] An attempt of identification of the AdC on Au was done by Barr and Seal[2b] who concluded that it mainly consists of physisorbed polymeric hydrocarbons containing an oxidized fraction that accounts for 10% to 30% of the total AdC. However, when a SC Au sample is exposed to air for ambient contamination, it encounters many environments of different composition adding further complexity to the surface composition before the XPS measurement. As recently reported by Greczynski and Hultman,[2d] the atomic composition (C 1s, O 1s, N 1s, and F 1s) of AdC on Au surfaces during 1 day of storage in air, HV, and UHV, strongly depends on the environment. For example, no O-containing species were found to accumulate in UHV within XPS detection limits, while a significant O 1s signal was present in Au samples stored in both HV and air. As our work focuses more on the quantitative aspects and the timing required for the AdC to form in air, we refer the reader interested in the details of C 1s and O 1s XPS peak deconvolution analysis to the many exhaustive reports present in literature.[2b,d,29]

With the purpose of investigating the timescales of formation of the AdC layer, we quantified the amount of carbon contaminant species accumulating on the Au surface by monitoring the C 1s and O 1s signals from SC Au(111) on mica samples for different aging times, after 10 min, 3 days, and 3 months of aging at ambient conditions, by means of XPS (Figure 1d). The samples were cleaned under UHV conditions via repeated cycles of Ar^+ sputtering and thermal annealing (details in the Experimental Section). The sputtering and annealing cycles on SC Au samples were stopped when no contaminant species were detected by UHV-STM imaging and XPS (see Figure S2 in the Supporting Information). The compositional data, reported on a logarithmic time scale, show that a rapid decrease in the Au content occurs within the first 10 min, as the total content of C and O is around 20%, confirming that organic contaminant species readily adsorb on the surface.

A fast contamination process is somehow expected if we compare the carbon fraction (%*C*) after 10 min at ambient conditions ($\%C_{10\ \mathrm{min}} = 18\%$) with that obtained from an Au(111) surface decorated with a (partial) monolayer of poly(*p*-phenylene) (PPP) wires ($\%C_{\mathrm{PPP}} = 11\%$) starting from 4,4″-dibromo-*p*-terphenyl (DBTP).[35] This molecular system was chosen as a reference to estimate the signal from a monolayer of known carbon-based contaminant (further details are provided in Section S2 in the Supporting Information). The %*C* of the airborne contaminant layer after 10 min is comparable to the %*C* obtained from an ideal, fully covering, close-packed self-assembled structure of PPP on Au(111) (chemical composition data and C 1s spectra reported in Figure 1d and Figure S1b in the Supporting Information, respectively). The immediate adsorption of carbon contaminants on sputter-cleaned surfaces was similarly observed in polycrystalline silver samples.[26] Note that SC samples exposed for 10 min to ambient air remained for at least 3 h at pressures above 10^{-6} mbar (the time for transfer to ambient air plus the time required to pump down the fast entry chamber), thus having supplementary time to build-up the contamination layer. However, given the slightly higher %*C* and a doubled O:C ratio at 3 days (≈0.2) compared to that at 10 min (≈0.1), oxidized carbon species containing C—O—C and O—C=O groups could be adding up through oxidation mediated by environmental water and oxygen[2b] or via CO and CO_2 adsorption[2d] after the full coverage of the Au surface. The relatively small decrease of %Au that was observed after 3 days of aging (%Au ≈ 75%) suggests, instead, that the accumulation of additional contaminant species on the first overlayer occurs at a much slower rate. The Au fraction calculated after 3 months of aging is further decreased to about 60%, confirming that the contamination process at ambient conditions does not stop within a few days. After this longer period, the oxygen fraction increases above 10% highlighting the more severe effects of environmental oxidizing agents at prolonged exposures to ambient air.

Altogether, XPS, CA, and %*S* measurements provided unambiguous evidence that the formation of a contamination layer occurs within tens of minutes after exposure to ambient conditions. The rapid initial drop of the WF can be explained by means of these techniques, however, none of them is able to elucidate why the WF starts to increase after the first few hours of aging. In other words, the second part of the curve needs a more accurate description of the AdC layer in order to be explained.

2.2. Dynamics of Surface Contamination of Au(111) at Ambient Conditions

The topography of Au(111) on mica samples is characterized by atomically flat terraces that are suitable to study the dynamics of formation of the AdC contamination. The AFM images reported in **Figure 2**a,b were recorded in noncontact mode and illustrate the effect of the aging on Au(111) after 3 h and 3 days from the transfer to ambient air, respectively. The monitoring of the surface contamination upon exposure to ambient air was done on SC Au(111) films supported on mica substrates. In the inset of Figure 2a, many terraces with steps in height *h* of 1–2 Å can be observed on the Au(111) surface (with the *z*-noise on atomically flat regions of the Au(111) terraces being around 0.4 Å). These topographic features can be ascribed to the accumulation of AdC and to the subsequent formation of individual objects, here referred to as contaminant aggregates or clusters.

The height and size of these aggregates increase with time, as observed upon monitoring the surface after 3 days (inset of Figure 2b). In some cases, the height of the aggregates exceeded 1 nm (range 0.5–1.9 nm). These aggregates can be either found close to a terrace edge or at an inner region of the terrace and their relative position within a terrace can affect their mobility. The migration dynamics of contaminant aggregates is better visualized through the movie available in Video S1 in the Supporting Information. This movie shows that aggregates can migrate within the terrace and two nearby aggregates can merge. Aggregates at a terrace edge tend to remain at their position, while aggregates at inner regions of the terraces may exhibit displacements of tens of nanometers in successively recorded images (each frame corresponds to ≈45 min in real time). The occurrence of these events reveals the dynamic nature of contaminants adsorbed onto Au(111) surfaces. In order to provide further demonstration that the contamination of Au(111) surfaces mediated by airborne contaminant species may occur ubiquitously, we compared the AFM topography of samples that were independently aged in two different laboratories (the first one placed in Padova and the second one in Strasbourg; see Figure S3 in the Supporting Information) for three weeks at ambient conditions. In both cases, thermally evaporated Au(111) on mica samples "as

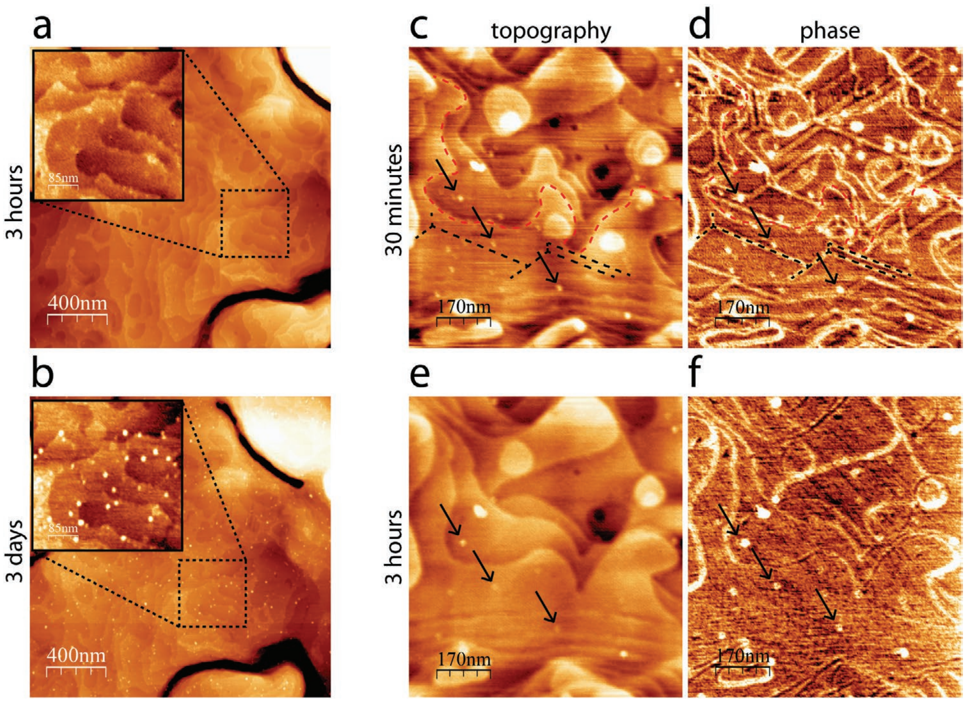

Figure 2. Ambient-AFM topography images of a SC Au(111) on mica surface collected in noncontact mode after a) 3 h and b) 3 days of aging at ambient conditions. A magnification of the same dashed area is provided in the inset of the images. Ambient-AFM c,e) topography and d,f) phase contrast images of a TS Au(111) surface collected in intermittent contact mode c,d) at $t = 30$ min and e,f) $t = 3$ h from peeling-off. Contaminant aggregates are indicated by black arrows. An example of terrace edge profile is indicated by a red dashed curved line, while the ⟨112⟩ directions are indicated by black dashed straight segments. The *Z*-scale is: a) 4.3 nm, b) 5.1 nm, c) 1.8 nm, d) 2°, e) 2.0 nm, and f) 2°. The number density of aggregates in (b) is n_s: 350 µm^{-2}. The entire sequence of the images is provided in Videos S1 and S2 in the Supporting Information.

received" from the manufacturer were imaged before and after an aging period of 3 weeks, without prior cleaning. Despite the possible differences in surface composition, arising from the presence of diverse contaminant species in the ambient air of the two laboratories, a similar growth of airborne contaminant aggregates in both laboratories is confirmed by the AFM topography images.

However, by using "as received" samples, no information about the first minutes of contamination after the ambient exposure is known. Likewise, by using SC Au, it is possible to investigate the contamination dynamics at a timescale shorter than the time required for the venting procedures of the vacuum chamber and the transfer to the AFM stage (that typically lasts ≈2 h). During this time period, the SC samples suffer from the exposure to the contaminant species entering in the vacuum chamber. Therefore, to circumvent such problems, we employed TS Au(111) to study the contamination processes as soon as the "clean" surface was exposed to ambient air.

The nucleation of contaminant aggregates starts to occur since the first minutes of air exposure, as it can be seen in Figure 2c–f where round-shaped objects, having a positive phase shift and marked by black arrows, are already found at t = 30 min with heights similar to those in the inset of Figure 2a. A different phase response is recorded when the tip scans an aggregate as shown in Figure S4 in the Supporting Information. Under our experimental conditions (intermittent contact mode in the attractive regime), a positive phase shift is expected for an increasing sample viscosity and a decreasing elastic modulus[36] in agreement with the aggregates being amorphous clusters of organic species.

As evidenced in Video S2 in the Supporting Information, during the first hours of aging of the TS Au sample, we also observed the modification of the surface, arising from the contamination process and/or the relaxation of the mechanical stress induced by the peel-off procedure. Indeed, the comparison of the topography image after 30 min, Figure 2c, and after 3 h, Figure 2e, shows that the smallest Au ad-islands and the step edges with the smallest curvature radius are disappearing because they are included in the surface (part 3 of Video S2 in the Supporting Information). Moreover, the phase image reported in Figure 2d is characterized by bright positive-shifted curved lines that can be attributed to the step edges (red dashed line in Figure 2d) but also by the presence of some unexpected straight lines aligned along the three ⟨112⟩ directions of Au(111) (black dashed lines in Figure 2d) that are barely visible in the topography images. The nature of these straight lines seems to be related to linear lattice defects. Indeed, as evidenced in the part 3 of Video S2 in the Supporting Information, these linear features move and reorganize until, after 3 h, they almost disappear, as evident in Figure 2f. To the best of our knowledge, there is only one previous example which demonstrates that defective regions can induce a change in the surface mechanical properties that can be resolved by phase imaging.[37] Therefore, the freshly TS Au shows a low level of AFM-visible contaminant aggregates but a large number of structural defects.

The above-discussed AFM images well summarize the surface processes occurring during aging and help us to describe the AdC layer as a dynamic system consisting of an overlayer of contaminant species that can accumulate into mobile contaminant aggregates. Interestingly, the surface modification is occurring at around the same aging time of the CPD bump and CPD curve minimum, thereby suggesting that the structural rearrangement of the gold surface and its AdC layer may also have an impact on the observed WF on the hour timescale.

2.3. Lateral Size Correction of Contaminant Aggregates Imaged via AFM

In order to quantify the real width of the features imaged by AFM, it is necessary to take into account the lateral broadening effect due to the finite size of the tip. Moreover, more pronounced effects may arise from tip degradation due to the long imaging times, yet the use of a noncontact imaging mode helps to preserve the integrity of the tip. Contaminant aggregates grew in lateral size (*d*) and height (*h*) during the aging period and the increase in their apparent lateral size (d_{app}) is not simply related to tip deterioration. In general, if the experimental AFM topography is affected by the tip convolution artifact, only apparent values for lateral size (d_{app}) and height (h_{app}) can be measured. To quantify the effective *d* of the aggregates, a simple geometrical correction model has been employed in order to remove the profile broadening (Δ) due to the finite size of the tip.[38] The mathematical derivation of the correction model is summarized in Section S4 in the Supporting Information.

For the sake of example, we applied the correction model to two aggregates: one imaged via noncontact mode (**Figure 3**a) and one imaged via intermittent contact mode (Figure 3b). Contaminant aggregates on gold can be described by a spherical cap of height *h* and lateral size *d* (see Figure 3e). The lateral size *d* after correction evaluates to 18 ± 3 nm and 25 ± 3 nm, for the cyan and blue profiles reported in Figure 3c. The two examples considered, differing in the AFM imaging mode and probe type, show aggregates that are significantly unalike in

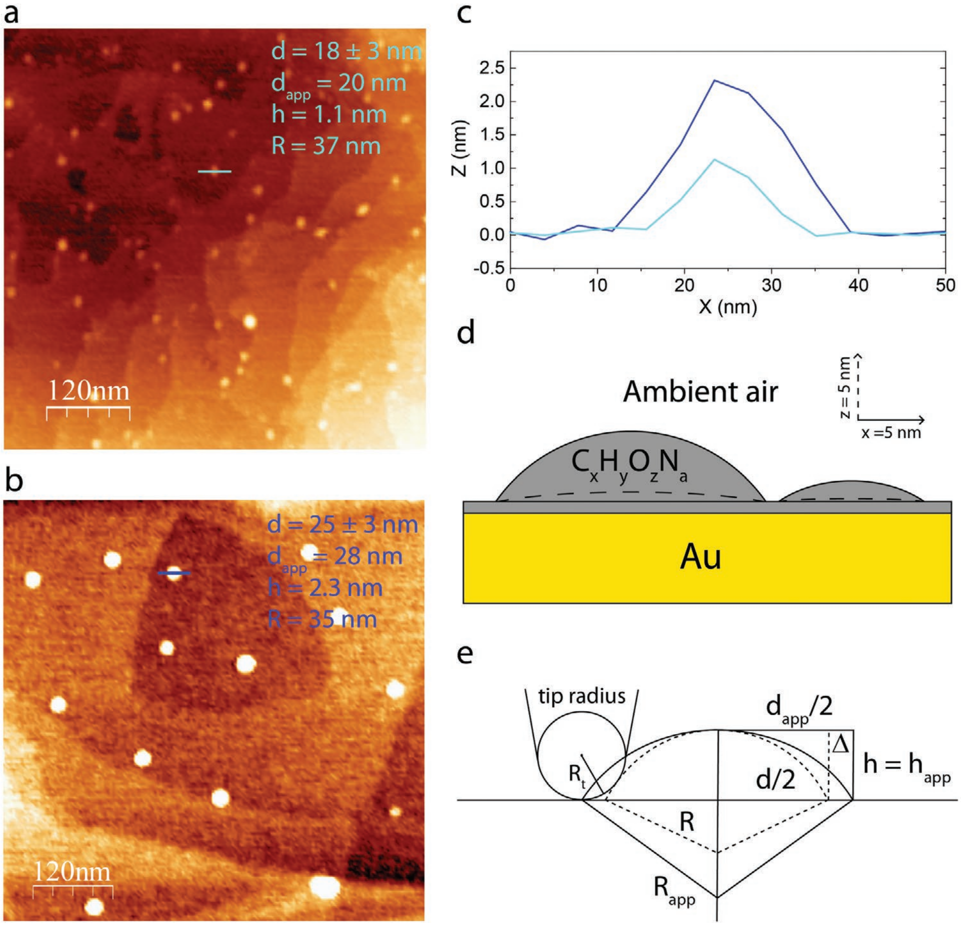

Figure 3. Ambient-AFM topography images of two contaminated Au(111) surfaces a) recorded in noncontact mode, magnification from Figure 2b, and b) recorded in intermittent contact mode, magnification from Figure S4c in the Supporting Information. *Z*-scale: a,b) 2.9 nm. c) Height profiles of the typical contaminant aggregates that are also indicated with cyan and blue horizontal lines in (a) and (b), respectively. d) Schematic image of an ideally flat Au surface with a uniform contamination layer with contaminant aggregates on top at the interface with ambient air. e) Geometrical model for the determination of the profile broadening due to the finite size of the tip. *R*, *h*, and *d* are the curvature radius, the height, and the lateral size of the aggregate, whereas R_{app}, h_{app}, and d_{app} are the corresponding apparent parameters. R_t is the tip radius and $2\Delta = d_{app} - d$ is the effective profile broadening.

lateral size after correction. Note here that the geometry of the aggregates is much "more flat" than it appears in the profiles. In the cartoon of Figure 3d, we propose a simplified picture of the microscopic geometry that characterizes the airborne contamination of Au(111) surfaces, where the "real" size aggregate is indicated with a dashed profile. The geometrical parameters listed in Table S2 in the Supporting Information (refer to the reported AFM images) show a clear increasing trend of d with increasing h. More details about the differences between noncontact and intermittent-contact imaging modes are provided in Section S4 in the Supporting Information. As a reference to the reader, the range of geometrical parameters characteristic of the aggregates in each figure is reported in Table S3 in the Supporting Information.

2.4. Scanning Electron Microscopy (SEM) Imaging and Energy-Dispersive X-Ray Spectroscopy (EDX)

To further characterize the AdC layer on Au(111) surfaces, we performed SEM imaging in specific areas of the sample, which were subsequently imaged by AFM. For this purpose, the samples were aged at ambient conditions until the contaminant aggregates were sufficiently large compared to the SEM lateral resolution. The surface topography of a contaminated Au sample was first obtained via SEM, by collecting the secondary electrons (**Figure 4**a), and then via AFM (Figure 4b). The aggregates monitored in the AFM image could be identified in the SEM image as darker spots, confirming the presence of aggregates with 30 nm < d < 80 nm. Grain boundaries were employed as topographical markers, enabling the imaging of the very same region by AFM and SEM, thereby providing a direct comparison between the two types of images (the method for searching the same sample region is illustrated in Section S5 and Figure S8 in the Supporting Information). The EDX spectra was also recorded to obtain information about the chemical composition of the contaminant layer. Such measurements revealed a predominance of C, N, and O elements onto the gold surface (see Figure S9 in the Supporting Information).

2.5. KPFM Measurements

With the aim of clarifying the role of contaminant aggregates on the WF increase, we measured the local CPD via KPFM. The presence of airborne contaminant aggregates induces a local change in the surface potential (SP) that is larger than the potential resolution (being below 10 mV),[39] as shown in **Figure 5**. For a metallic surface, the average CPD can be directly correlated to the SP or to the WF of the sample and a quite negligible correlation between the topography and the CPD images is expected for an oriented Au(111) sample. In particular, the CPD change associated with the height variation at a grain boundary (dark area in Figure 5a, around 20 nm dip) is comparable with the background noise, while 20 nm thick aggregates exhibit CPD variations of ΔCPD ≈ −25 mV, as indicated by the profiles in Figure 5c.

However, the determination of the effective SP of a single nanometric aggregate is limited by the long-range electrostatic interactions ($\approx d^{-2}$) between the tip and the surface.[40] In the case of metallic samples, the electrostatic interaction only affects the surface and thus, solely the structures at the surface contribute to the measured potential.[22a] In general, the lateral resolution of KPFM is on the order of a few tens of nanometers[39] and in the KPFM images reported here the achieved resolution is ≈50 nm. Thus, when the lateral size of the nanostructure is below 100 nm, the corresponding measured potential is underestimated, being the average of the effective value of the nanostructure and that of the surrounding substrate.[22a] Such effect is visible in the upper-left side of Figure 5b, where aggregates are smaller and present in greater amount compared to the right side of the CPD image. In this region, the averaging effect dominates, thereby not allowing to measure significant potential variations. The smaller CPD of airborne contaminant aggregates compared to the rest of the surface suggests that electrons are withdrawn from the metal and accumulated at the metal/dielectric interface, as local surface charge densities can be detected via KPFM for charged defects that are at least 50 nm apart.[41] If the average CPD of the image at increasing aging

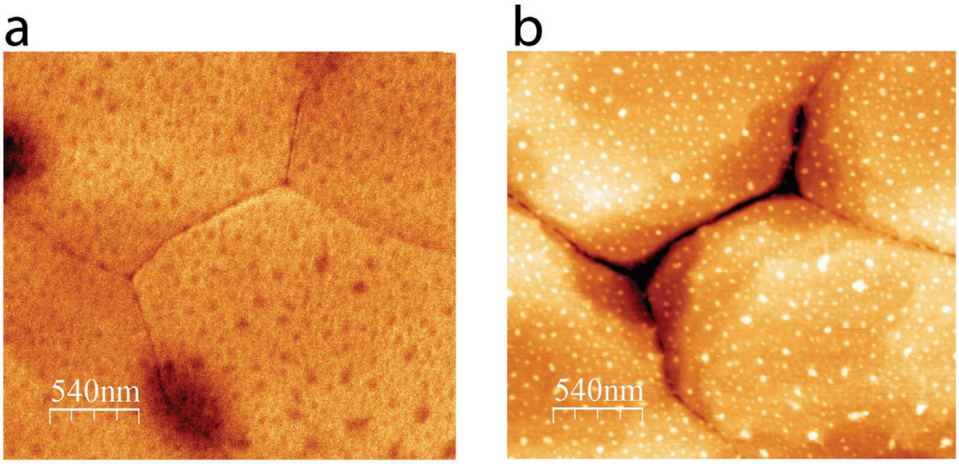

Figure 4. a) SEM topography obtained from a Au(111) on mica sample after a long aging (>3 months) with the secondary electrons detector, the acceleration voltage set at 20 kV, dwell time at 10 µs, and chamber pressure $\approx 10^{-6}$ mbar. b) Corresponding AFM topography collected at ambient conditions. Z-scale: 17.0 nm; n_s: 350 µm^{-2}.

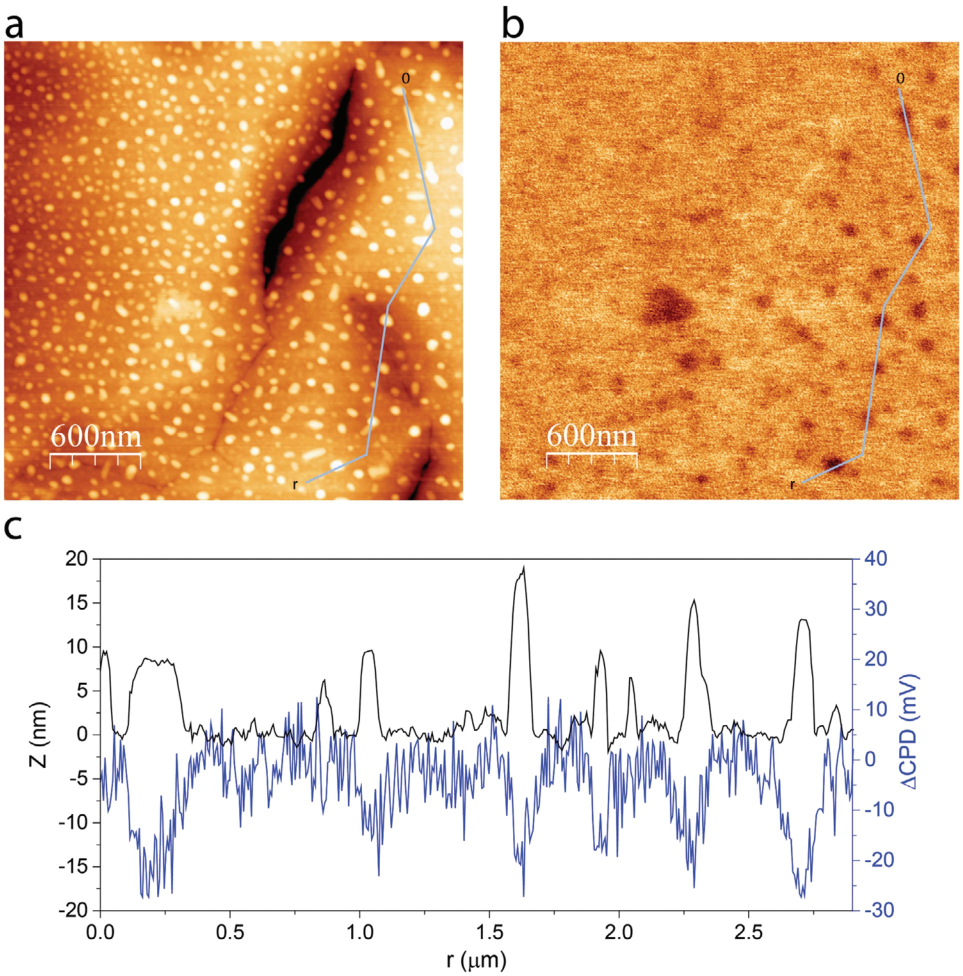

Figure 5. a) Surface topography versus b) CPD difference (3 × 3 µm^2) from a Au(111) on mica surface after a long aging (>3 months) at laboratory conditions collected by amplitude-modulation KPFM in Bologna. The sample "as received" was aged at ambient conditions without prior cleaning. The *Z*-scale: a) 34.2 nm, b) 43.6 mV; n_s: 200 µm^{-2}. c) Height (black) and ΔCPD (blue) profiles along the path indicated with a gray line on the images above. The contribution of the substrate to the height profile was removed with a background subtraction to highlight the correspondence between height and CPD peaks.

times is considered instead, we found as well an increasing CPD, as visible in Figure S10 in the Supporting Information. Hence, the contribution of the contaminant aggregates to the WF cannot be separated from the overall measured value, which is determined by the ensemble of Au(111) and the AdC layer.

2.6. Effect of Storage Conditions

The storage of Au(111) samples in closed environments, where the supply of contaminant aggregates inside the volume of the container is limited, revealed other peculiarities of contaminated Au(111) on mica surfaces. One obvious way to slow down the growth of the AdC layer is by placing the samples inside a sealed container at ambient conditions. For this purpose, we compared the sample "as received" from the manufacturer (**Figure 6**a) and a sample from the same batch that was stored for 8 months in the storage container (Figure 6b). Note that the small container (≈50 cm^3) was occasionally opened for few minutes and then sealed again without any gas purging. These storage conditions represent the ordinary laboratory use of Au on mica samples. The size of contaminant aggregates found in the 8-month sample is larger while the number density (n_s) is still low (n_s = 40 µm^{-2}) compared to that recorded in an open-air system during the first days of contamination (Figure 2b). Aggregation processes are thus dominant over novel nucleation events of contaminant clusters when gold is stored in a closed environment of reduced dimensions. This example highlights the slowing-down effects of the storage in a sealed container on the growth of aggregates. While ambient air is a potentially infinite reservoir of contaminants, the absorption of contaminant species and the growth of aggregates causes the partial pressure of these contaminants to drop in the storage container.

A further evidence of the growth and aggregation phenomena occurring during the storage in closed environments is that the n_s of clusters tends to diminish while clusters increase in size. The AFM topography of a heavily contaminated sample before (Figure 6c) and after (Figure 6d) 2 days

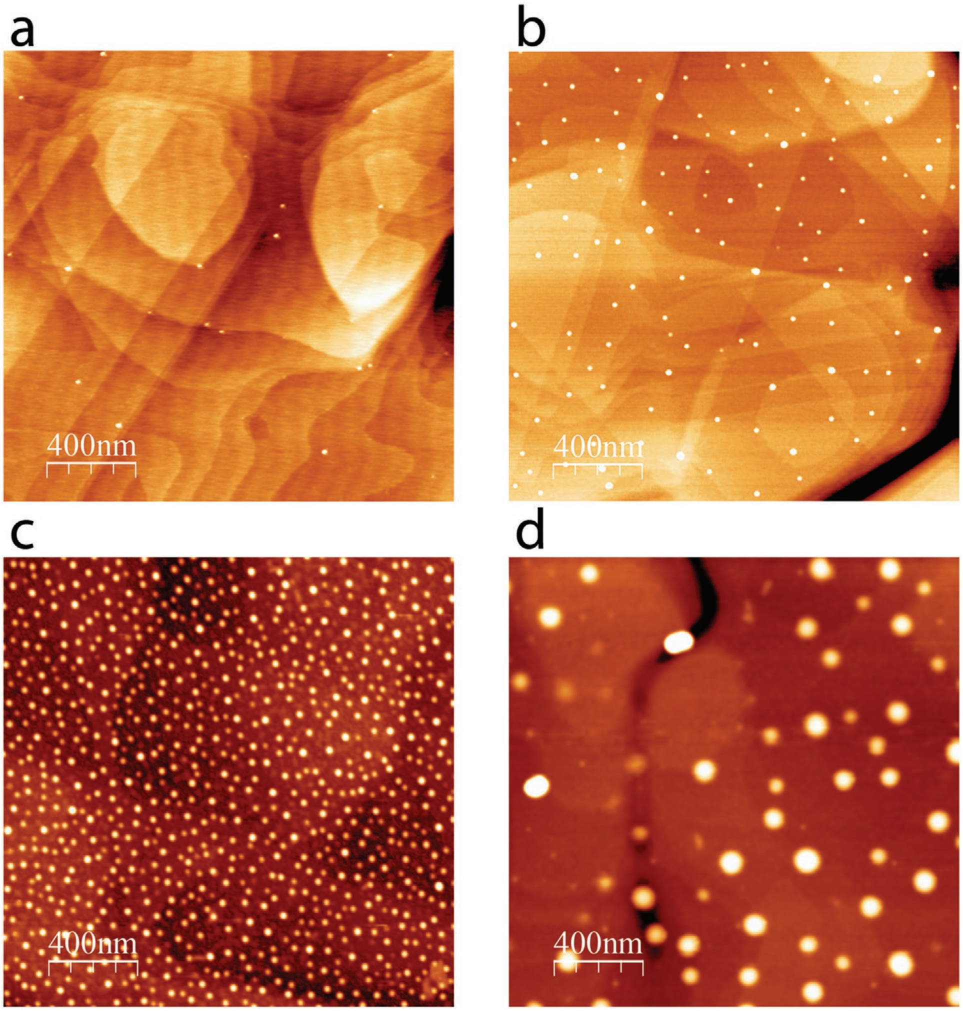

Figure 6. Ambient-AFM topography of contaminated Au(111) on mica a) "as received" from the manufacturer and b) after 8 months of storage in a closed and sealed container that was occasionally opened during laboratory activity. Effect of closing an AdC contaminated Au(111) sample inside a sealed container for 2 days, c) before and d) after. AFM topography of *Z*-scale: a) 2.5 nm, b) 8.9 nm, c) 10 nm, and d) 18 nm; n_S: a) 15 µm^{-2}, b) 40 µm^{-2}, c) 300 µm^{-2}, and d) 40 µm^{-2}.

of storage inside a closed glass container is a clear example of the above-mentioned effect. We then measured the WF of TS Au(111) samples after repetitive cycles of 2-day storage in open (laboratory air) and closed environments (glass container). The change of the average WF and absolute PY slope is reported in **Figure 7**. The WF of samples in "closed" conditions was immediately measured after exposure (within 10 min). The WF consistently increased by ≈0.3 eV when the sample was exposed to laboratory air and decreased by ≈0.3 eV during storage in a closed container. The concomitant increase of the PY when samples were stored in closed conditions indicates that a significant fraction of the surface that was previously covered by aggregates then became uncovered. The growth of aggregates does not stop when the sample is enclosed in a sealed container because the aggregation keeps taking place while the nucleation is hindered. The surface mechanism explaining the observed trend of PY slope is the migration and merging of contaminant aggregates shown in Video S1 in the Supporting Information. This final example demonstrates the active contribution of contaminant aggregates to the change of the Au(111) WF.

By and large, the two phases of surface contamination of Au(111) have a strikingly different impact on the WF, driving the WF change in opposite directions. During the first phase, the rapid change of the WF is due to the adsorption of contaminants. Subsequently, the growth and aggregation of contaminant clusters provides a mechanism for segregation of molecular contaminants at the gold/air interface, which significantly affects the observed WF values. The long exposure of gold samples to ambient conditions leads to an increase of the WF with respect to the minimum observed in the KP and PYS curves. The interaction at the interface between the Au surface and the contaminant aggregates underlies the increment in the average WF that can thus be explained by considering the metal/dielectric (aggregates) system as a whole. When putting the sample in an open/closed environment a reversible change in WF was measured, revealing the dynamic reorganization of the contaminated gold surface mediated by the aggregates.

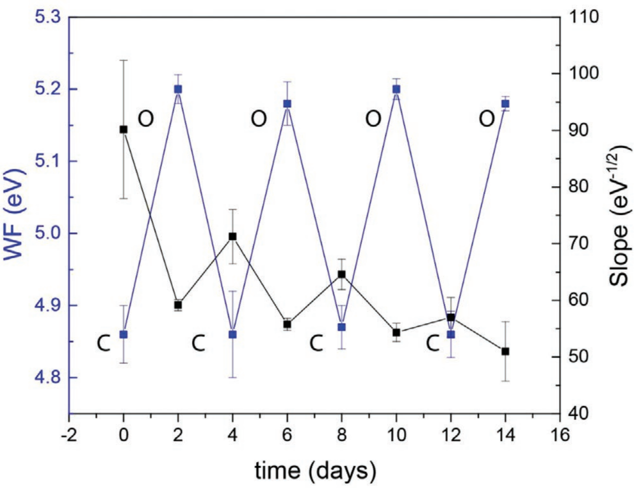

Figure 7. WF (black squares) versus PY slope (blue squares) changes of Au(111) on mica upon cycles of exposure to ambient conditions and closing in a glass container. O and C letters in the graph indicate the storage conditions (O = open laboratory air; C = closed in a glass container).

3. Conclusions

The physical and chemical properties of gold surfaces are dynamic, as they strongly depend on the surrounding environment. Alongside the well-known and documented surface reconstruction of the thermodynamically unstable Au(111) surface,[42] the surface topography, composition, and work function are found to change upon aging the samples in ambient air. The WF of clean Au was found to decrease by an average of 0.5 eV within a few hours when transferred to ambient conditions and then slowly recovered a value approaching the original WF after a few weeks. We shed light over the disregarded phenomena of the airborne contamination of gold by unraveling the dynamic nature of Au(111), which showed a surface reorganization of the AdC overlayer and an efficient segregation of contaminant species into aggregates. Two separate contamination regimes were identified: a starting rapid phase, where contaminant species are readily adsorbed within minutes from exposure to ambient air and reorganize on the surface, and a slow phase, during which carbon species accumulate over time while contaminant clusters migrate and grow via aggregation. Previously unexplained WF variations have been rationalized via a multiscale and multitechnique approach, which revealed the presence and growth of contaminant aggregates on the Au(111) surface. While surface contamination is often overlooked because of its intrinsic variability, we demonstrated the universal nature of our studies on Au(111) by pointing out the common behavior of gold samples upon aging at ambient conditions.

Our findings are relevant for both experimental and theoretical purposes. Since clean gold exhibits unstable surface properties, and an exposure to air of a few weeks is required in order to obtain a gold surface with stable properties, this implies, for instance, that an equilibration period at ambient conditions must be included for KP or KPFM tip calibration. The generally wrong claim regarding the inert nature of gold accompanied by a stable WF holds true only after a careful preparation and storage of the reference sample. Moreover, we provided a simple picture for the geometrical modeling of contamination, useful for signal correction in X-ray techniques (e.g., XPS, EDX, and XRR), and we first reported on the effect of the contamination dynamics on the Au WF. Such understanding is critical for applications where planar bare gold is employed, such as charge control via UV photoemission in space-based systems (LISA[43] and TianQin[44]) or charge injection at semiconductor/electrode interfaces. Hence, our findings are key for applications based on Au electrodes, e.g., in biosensing (SPR), optoelectronics, etc.

4. Experimental Section

Preparation of Au(111) on Mica Samples in UHV: Commercially available epitaxial Au(111) thin films grown on mica substrates manufactured by Phasis (Geneva, Switzerland) were transferred in a UHV chamber kept at a base pressure $p \approx 10^{-9}$ mbar. The samples were cleaned via repeated cycles of sputtering and annealing at 400 °C and the surface composition was monitored via XPS until the absence of C 1s and O 1s signals was achieved. The absence of residual contaminant aggregates was further confirmed via in situ STM imaging (see Figure S1a in the Supporting Information). The sputter-cleaning was performed with an Ar^+ ion gun set at an accelerating voltage of 1.5 kV and at a chamber pressure $p = 4.5 \times 10^{-6}$ mbar. After cleaning, the samples were transferred to ambient air and kept stored inside open containers at ambient conditions when not used for analysis.

Aging of Au(111) on Mica Samples: Aging experiments in Strasbourg were done by using epitaxial Au(111) thin films grown on mica (Georg Albert PVD, Heidelberg, Germany). Au samples were used both "as received," hence with a pre-existing contamination layer, or after peeling off with biadhesive copper tape, thus exhibiting the "clean" side of the Au film. The Au films on the copper tape were then stuck on the backside of Si wafers to obtain a flat sample for AFM imaging and contact angle measurements. The contact angle of mica was below 10° and that of copper tape was above 115°.

Instrumentation: AFM measurements were performed in Padova and in Strasbourg. In Padova, the AFM images were recorded at ambient conditions with an Agilent 5500 Scanning Probe Microscope equipped with an Agilent N9521A scanner. The vertical noise declared by the manufacturer (0.5 Å RMS) was in accordance with the experimental observations. The measurements were performed in noncontact mode with NanoWorld NCSTR probes (tip radius = 8 ± 3 nm, resonant frequency ≈160 kHz, $k \approx 7.4$ N m^{-1}). In Strasbourg, the AFM images were recorded in intermittent contact mode at ambient conditions with a Bruker Multimode (Bruker Tespa-V2 probes, tip radius = 10 ± 3 nm, resonant frequency ≈320 kHz, $k \approx 32$ N m^{-1}). Phase contrast and associated topography images were collected in intermittent contact mode at ambient conditions with a Bruker Dimension Icon AFM (Bruker Tespa-V2 probes) equipped with an optical microscope.

The Multimode AFM, equipped with an Extender Electronics module, was employed for KPFM experiments. Topography and CPD images were simultaneously collected at ambient conditions with Pt/Ir coated silicon probes (Bruker SCM-PIT, resonant frequency ≈75 kHz, $k \approx 2.8$ N m^{-1}). The KPFM data presented in this work was acquired in the amplitude modulation mode. The SPM image processing was done on WSxM software.[45] KP measurements were performed at ambient conditions on "as received" Au(111) on mica samples using a 2 mm diameter gold tip amplifier (Ambient Kelvin Probe Package from KP Technology, Ltd.). The calibration of the probe was performed against a freshly cleaved HOPG surface.[46] PY curves were recorded using a Riken Keiki spectrophotometer (Japan) model AC-2. The instrument was operated with an energy step of 0.05 eV and a UV spot intensity of 50 nW. SEM imaging was performed with an FEI Quanta FEG 250 operated at an accelerating voltage of 20 kV and at pressures below 10^{-6} mbar. The SEM images were collected with the detector for secondary electrons. Contact angle of sessile water drops on gold surfaces was measured with a Krüss DSA100 Drop Shape Analyser.

XPS spectra were recorded at room temperature at a base pressure of 10^{-9} mbar using a VG Scienta XM 650 X-ray source operated at 12 kV and 30 mA. The X-rays were monochromatized using a VG Scienta XM 780 monochromator optimized for Al Kα radiation (1486.7 eV). Photoelectrons were collected at normal incidence and analyzed with a Scienta SES 100 hemispherical electron analyzer operated at constant pass energy of 200 eV. The wide range spectra were collected with an energy step of 2 eV. Au $4f_{7/2}$ signal at 84.0 eV was used to calibrate the binding energy scale of the XPS spectra. Peak areas were calculated from Au 4f, C 1s, and O 1s signals according to the Shirley method.[47] Relative peak area ratios expressed as atomic percentages were calculated from reference atomic sensitivity factors (ASFs)[48] and accounting for the transmission properties of the analyzer. After cleaning the surface with sputtering and annealing cycles, the Au(111) on mica samples were transferred to the ambient environment and stored in an open container for a fixed amount of time before the XPS measurement. The samples were transferred again inside the UHV system through a prechamber, pumped down to 10^{-6} mbar within 1 h, and then moved to the main chamber.

Supporting Information

Supporting Information is available from the Wiley Online Library or from the author.

Acknowledgements

The work in Strasbourg was financially supported by EC through the ERC project SUPRA2DMAT (GA-833707), the Marie Curie ITN project UHMob (GA-811284), the Labex projects CSC (ANR-10-LABX-0026 CSC), and NIE (ANR-11-LABX-0058 NIE) within the Investissement d'Avenir program ANR-10-IDEX-0002-02, and the International Center for Frontier Research in Chemistry (icFRC). N.T. thanks Alex Boschi (CNR-ISOF/Italy) for the help with the calculation of statistical parameters from the AFM images, Francesco de Boni (University of Padova/Italy) for the experimental support with the UHV system and Manveer Gill for the text revision.

Conflict of Interest

The authors declare no conflict of interest.

Data Availability Statement

Data available on request from the authors.

Keywords

adventitious carbon, gold, Kelvin probe, photoemission yield, surface contamination, work function

Received: January 13, 2021
Revised: February 16, 2021
Published online: March 23, 2021

[1] T. Smith, *J. Colloid Interface Sci.* **1980**, *75*, 51.
[2] a) C. D. Wagner, *J. Electron Spectrosc. Relat. Phenom.* **1980**, *18*, 345; b) T. L. Barr, S. Seal, *J. Vac. Sci. Technol., A* **1995**, *13*, 1239; c) A. Fahlman, C. Nordling, K. Siegbahn, *ESCA: Atomic, Molecular and Solid State Structure Studied by Means of Electron Spectroscopy*, Almqvist & Wiksell, Uppsala, Sweden **1967**; d) G. Greczynski, L. Hultman, *Prog. Mater. Sci.* **2020**, *107*, 100591.
[3] a) M. A. Baker, *Thin Solid Films* **1980**, *69*, 359; b) A. Wan, J. Hwang, F. Amy, A. Kahn, *Org. Electron.* **2005**, *6*, 47; c) H. Piao, N. S. McIntyre, *Surf. Interface Anal.* **2002**, *33*, 591.
[4] a) M. P. Seah, S. J. Spencer, *J. Vac. Sci. Technol., A* **2003**, *21*, 345; b) F. Sugimoto, S. Okamura, *J. Electrochem. Soc.* **1999**, *146*, 2725; c) E. L. Strein, D. Allred, *Thin Solid Films* **2008**, *517*, 1011; d) Y. Azuma, A. Kurokawa, *X-Ray Spectrom.* **2019**, *48*, 345.
[5] a) P. K. Biswas, A. De, L. K. Dua, L. Chkoda, *Appl. Surf. Sci.* **2006**, *253*, 1953; b) K. Sugiyama, H. Ishii, Y. Ouchi, K. Seki, *J. Appl. Phys.* **1999**, *87*, 295.
[6] a) B. R. Strohmeier, *J. Adhes. Sci. Technol.* **1992**, *6*, 703; b) M. Mantel, J. P. Wightman, *Surf. Interface Anal.* **1994**, *21*, 595; c) M. E. Schrader, *J. Phys. Chem.* **1970**, *74*, 2313.
[7] S. Buchman, T. Quinn, G. M. Keiser, D. Gill, T. J. Sumner, *Rev. Sci. Instrum.* **1995**, *66*, 120.
[8] S. Saraf, S. Buchman, K. Balakrishnan, C. Y. Lui, M. Soulage, D. Faied, J. Hanson, K. Ling, B. Jaroux, B. A. Suwaidan, A. AlRashed, B. Al-Nassban, F. Alaqeel, M. A. Harbi, B. B. Salamah, M. B. Othman, B. B. Qasim, A. Alfauwaz, M. Al-Majed, D. DeBra, R. Byer, *Classical Quantum Gravity* **2016**, *33*, 245004.
[9] M. Armano, H. Audley, G. Auger, J. T. Baird, M. Bassan, P. Binetruy, M. Born, D. Bortoluzzi, N. Brandt, M. Caleno, L. Carbone, A. Cavalleri, A. Cesarini, G. Ciani, G. Congedo, A. M. Cruise, K. Danzmann, M. de Deus Silva, R. De Rosa, M. Diaz-Aguiló, L. Di Fiore, I. Diepholz, G. Dixon, R. Dolesi, N. Dunbar, L. Ferraioli, V. Ferroni, W. Fichter, E. D. Fitzsimons, R. Flatscher, et al, *Phys. Rev. Lett.* **2016**, *116*, 231101.
[10] a) L. Chai, J. Klein, *Langmuir* **2007**, *23*, 7777; b) S. Müllegger, A. Winkler, *Surf. Sci.* **2005**, *574*, 322.
[11] a) C. E. Taylor, S. D. Garvey, J. E. Pemberton, *Anal. Chem.* **1996**, *68*, 2401; b) S. Hüfner, R. L. Cohen, G. K. Wertheim, *Phys. Scr.* **1972**, *5*, 91; c) E. Taglauer, *Appl. Phys. A* **1990**, *51*, 238.
[12] J. Kang, P. A. Rowntree, *Langmuir* **2007**, *23*, 509.
[13] a) M. Adamov, B. Perović, T. Nenadović, *Thin Solid Films* **1974**, *24*, 89; b) A. I. Stognij, N. N. Novitskii, S. D. Tushina, S. V. Kalinnikov, *Tech. Phys.* **2003**, *48*, 745.
[14] C. Nogues, M. Wanunu, *Surf. Sci.* **2004**, *573*, L383.
[15] a) M.-Y. Tsai, J.-C. Lin, *J. Colloid Interface Sci.* **2001**, *238*, 259; b) D. F. O'Kane, K. L. Mittal, *J. Vac. Sci. Technol.* **1974**, *11*, 567; c) P. Fuchs, *Appl. Surf. Sci.* **2009**, *256*, 1382.
[16] a) D. E. King, *J. Vac. Sci. Technol., A* **1995**, *13*, 1247; b) S. Rentenberger, A. Vollmer, E. Zojer, R. Schennach, N. Koch, *J. Appl. Phys.* **2006**, *100*, 053701; c) D. W. Moon, A. Kurokawa, S. Ichimura, H. W. Lee, I. C. Jeon, *J. Vac. Sci. Technol., A* **1999**, *17*, 150.
[17] Z. Yang, A. Gonzalez-Cortes, G. Jourquin, J.-C. Viré, J.-M. Kauffmann, J.-L. Delplancke, *Biosens. Bioelectron.* **1995**, *10*, 789.
[18] a) L.-H. Guo, J. S. Facci, G. McLendon, R. Mosher, *Langmuir* **1994**, *10*, 4588; b) L. M. Fischer, M. Tenje, A. R. Heiskanen, N. Masuda, J. Castillo, A. Bentien, J. Émneus, M. H. Jakobsen, A. Boisen, *Microelectron. Eng.* **2009**, *86*, 1282; c) R. F. Carvalhal, R. Sanches Freire, L. T. Kubota, *Electroanalysis* **2005**, *17*, 1251.
[19] D. Martinez-Martin, R. Longuinhos, J. G. Izquierdo, A. Marele, S. S. Alexandre, M. Jaafar, J. M. Gómez-Rodríguez, L. Bañares, J. M. Soler, J. Gomez-Herrero, *Carbon* **2013**, *61*, 33.
[20] J. Lecoeur, J. P. Bellier, C. Koehler, *Electrochim. Acta* **1990**, *35*, 1383.
[21] M. Chelvayohan, C. H. B. Mee, *J. Phys. C: Solid State Phys.* **1982**, *15*, 2305.

[22] a) A. Liscio, V. Palermo, O. Fenwick, S. Braun, K. Müllen, M. Fahlman, F. Cacialli, P. Samorí, *Small* **2011**, *7*, 634; b) I. D. Baikie, A. C. Grain, J. Sutherland, J. Law, *Appl. Surf. Sci.* **2014**, *323*, 45; c) J. S. Kim, B. Lägel, E. Moons, N. Johansson, I. D. Baikie, W. R. Salaneck, R. H. Friend, F. Cacialli, *Synth. Met.* **2000**, *111–112*, 311.

[23] a) J. Landoulsi, M. J. Genet, S. Fleith, Y. Touré, I. Liascukiene, C. Méthivier, P. G. Rouxhet, *Appl. Surf. Sci.* **2016**, *383*, 71; b) G. C. Smith, *J. Electron Spectrosc. Relat. Phenom.* **2005**, *148*, 21; c) S. Evans, *Surf. Interface Anal.* **1997**, *25*, 924; d) G. Vereecke, P. G. Rouxhet, *Surf. Interface Anal.* **1999**, *27*, 761.

[24] a) D. L. Gil, D. Windover, *J. Phys. D: Appl. Phys.* **2012**, *45*, 235301; b) C. Chauvet, F. Polack, M. G. Silly, B. Lagarde, M. Thomasset, S. Kubsky, J. P. Duval, P. Risterucci, B. Pilette, I. Yao, N. Bergeard, F. Sirotti, *J. Synchrotron Radiat.* **2011**, *18*, 761.

[25] a) A. Kahn, *Mater. Horiz.* **2016**, *3*, 7; b) M. Uda, Y. Nakagawa, T. Yamamoto, M. Kawasaki, A. Nakamura, T. Saito, K. Hirose, *J. Electron Spectrosc. Relat. Phenom.* **1998**, *88–91*, 767.

[26] W. M. H. Sachtler, G. J. H. Dorgelo, A. A. Holscher, *Surf. Sci.* **1966**, *5*, 221.

[27] A. Krozer, M. Rodahl, *J. Vac. Sci. Technol., A* **1997**, *15*, 1704.

[28] a) M. A. Chesters, G. A. Somorjai, *Surf. Sci.* **1975**, *52*, 21; b) S. M. Wetterer, D. J. Lavrich, T. Cummings, S. L. Bernasek, G. Scoles, *J. Phys. Chem. B* **1998**, *102*, 9266.

[29] S. Sinha, M. Mukherjee, *Vacuum* **2018**, *148*, 48.

[30] H. Ishii, H. Kinjo, T. Sato, S.-i. Machida, Y. Nakayama, *Electronic Processes in Organic Electronics: Bridging Nanostructure, Electronic States and Device Properties*, Springer, Tokyo **2015**, pp. 131–155.

[31] I. D. Baikie, P. J. Estrup, *Rev. Sci. Instrum.* **1998**, *69*, 3902.

[32] S. Kinoshita, T. Ohta, H. Kuroda, *Bull. Chem. Soc. Jpn.* **1976**, *49*, 1149.

[33] a) B. Friedel, T. J. K. Brenner, C. R. McNeill, U. Steiner, N. C. Greenham, *Org. Electron.* **2011**, *12*, 1736; b) T. Kagiyama, Y. Saito, K. Otobe, S. Nakajima, *Appl. Surf. Sci.* **2003**, *216*, 542.

[34] a) G. Greczynski, L. Hultman, *ChemPhysChem* **2017**, *18*, 1507; b) T. L. Barr, *J. Phys. Chem.* **1978**, *82*, 1801.

[35] A. Basagni, F. Sedona, C. A. Pignedoli, M. Cattelan, L. Nicolas, M. Casarin, M. Sambi, *J. Am. Chem. Soc.* **2015**, *137*, 1802.

[36] W. W. Scott, B. Bhushan, *Ultramicroscopy* **2003**, *97*, 151.

[37] A. Minj, D. Cavalcoli, A. Cavallini, P. Gamarra, M.-A. di Forte Poisson, *Nanotechnology* **2013**, *24*, 145701.

[38] a) B. M. Borkent, S. de Beer, F. Mugele, D. Lohse, *Langmuir* **2010**, *26*, 260; b) B. Song, W. Walczyk, H. Schönherr, *Langmuir* **2011**, *27*, 8223.

[39] A. Liscio, V. Palermo, K. Müllen, P. Samorì, *J. Phys. Chem. C* **2008**, *112*, 17368.

[40] A. Liscio, V. Palermo, P. Samorì, *Acc. Chem. Res.* **2010**, *43*, 541.

[41] Y. Rosenwaks, R. Shikler, T. Glatzel, S. Sadewasser, *Phys. Rev. B* **2004**, *70*, 085320.

[42] a) S. Narasimhan, D. Vanderbilt, *Phys. Rev. Lett.* **1992**, *69*, 1564; b) R. J. Needs, M. Mansfield, *J. Phys.: Condens. Matter* **1989**, *1*, 7555.

[43] a) P. J. Wass, D. Hollington, T. J. Sumner, F. Yang, M. Pfeil, *Rev. Sci. Instrum.* **2019**, *90*, 064501; b) G. Hechenblaikner, T. Ziegler, I. Biswas, C. Seibel, M. Schulze, N. Brandt, A. Schöll, P. Bergner, F. T. Reinert, *J. Appl. Phys.* **2012**, *111*, 124914.

[44] F. Yang, Y. Bai, W. Hong, H. Li, L. Liu, T. J. Sumner, Q. Yang, Y. Zhao, Z. Zhou, *Classical Quantum Gravity* **2020**, *37*, 115005.

[45] I. Horcas, R. Fernández, J. M. Gómez-Rodríguez, J. Colchero, J. Gómez-Herrero, A. M. Baro, *Rev. Sci. Instrum.* **2007**, *78*, 013705.

[46] W. N. Hansen, G. J. Hansen, *Surf. Sci.* **2001**, *481*, 172.

[47] D. A. Shirley, *Phys. Rev. B* **1972**, *5*, 4709.

[48] J. Chastain, *Handbook of X-Ray Photoelectron Spectroscopy*, Perkin-Elmer Corporation, Eden Prairie, MN **1992**, pp. 40–221.